Three-layer model for the surface second-harmonic generation yield including multiple reflections

Sean M. Anderson and Bernardo S. Mendoza*
Centro de Investigaciones en Óptica, León, Guanajuato, México
(Received 4 July 2016; revised manuscript received 9 September 2016; published 30 September 2016)

We present the three-layer model to calculate the surface second-harmonic generation (SSHG) yield. This model considers that the surface is represented by three regions or layers. The first layer is the vacuum region with a dielectric function $\epsilon_v(\omega) = 1$ from where the fundamental electric field impinges on the material. The second layer is a thin layer (ℓ) of thickness d characterized by a dielectric function $\epsilon_\ell(\omega)$, and it is in this layer where the SSHG takes place. The third layer is the bulk region denoted by b and characterized by $\epsilon_b(\omega)$. Both the vacuum and bulk layers are semi-infinite. The model includes the multiple reflections of both the fundamental and the second-harmonic (SH) fields that take place at the thin layer ℓ. We obtain explicit expressions for the SSHG yield for the commonly used s and p polarizations of the incoming 1ω and outgoing 2ω electric fields, where no assumptions for the symmetry of the surface are made. These symmetry assumptions ultimately determine which components of the surface nonlinear second-order susceptibility tensor $\boldsymbol{\chi}(-2\omega;\omega,\omega)$ are different from zero, and thus contribute to the SSHG yield. Then, we particularize the results for the most commonly investigated surfaces, the (001), (110), and (111) crystallographic faces, taking their symmetries into account. We use the three-layer model and compare it against the experimental results of a Si(111)(1×1):H surface, as a test case, and use it to predict the SSHG yield of a Si(001)(2×1) surface.

DOI: 10.1103/PhysRevB.94.115314

I. INTRODUCTION

Surface second-harmonic generation (SSHG) has been shown to be an effective, nondestructive, and noninvasive probe to study surface and interface properties [1–8]. SSHG spectroscopy is now very cost effective and popular because it is an efficient method for characterizing the properties of buried interfaces and nanostructures. The high surface sensitivity of SSHG spectroscopy is due to the fact that within the dipole approximation, the bulk second-harmonic generation (SHG) in centrosymmetric materials is identically zero. The SHG process can occur only at the surface where the inversion symmetry is broken. SSHG has useful applications for studying thick thermal oxides on semiconductor surfaces [9,10] and thin films [11]. The accurate determination of these studies is highly dependent on multiple reflections of both the SH and fundamental waves in the surface region. These considerations have been taken into account to study thin films [12–14] and, using the Maker fringe technique [15], other materials [16,17].

Reference [18] was the first to consider multiple reflections in their treatment of SHG in a nonlinear slab. However, they only considered the second-harmonic (SH) fields and derived results for a dielectric with a small linear reflectance. They also neglected the multiple reflections of the fundamental waves inside the media.

Surface effects were modeled by taking the limit of a thin slab with a thickness much smaller than the wavelength of the incoming light. Reference [19] used this methodology to determine the components of the nonlinear optical susceptibility tensor, $\boldsymbol{\chi}(-2\omega;\omega,\omega)$, of a fluorescent dye over fused silica. However, later works [20,21] developed a simplified method using phenomenological models in which the surface is treated as an infinitesimally thin dipole sheet. Alternatively, the procedure established in Ref. [22] calculates $\boldsymbol{\chi}(-2\omega;\omega,\omega)$, and at the same time, the radiated fields. The inclusion of multiple reflections is necessary for both the SH radiation and the incoming fundamental fields; this is later experimentally verified in Ref. [23], where they show that the line shape of the SSHG radiation is composed of resonances from both the SH and fundamental waves. Total internal reflection of these waves causes a Goos-Hänchen shift [24], a lateral shift of the reflected beam. This effect was predicted for SHG [25,26] and successfully observed in metallic metasurfaces [27].

As mentioned above, SSHG is particularly useful for studying the surfaces of centrosymmetric materials. From the theoretical point of view, the calculation of $\boldsymbol{\chi}(-2\omega;\omega,\omega)$ proceeds as follows. To mimic the semi-infinite system, we construct a supercell consisting of a finite slab of material plus a vacuum region. Both the size of the slab and the vacuum region should be such that the value of $\boldsymbol{\chi}(-2\omega;\omega,\omega)$ is well converged. A cut function is used to decouple the two halves of the supercell in order to obtain the value of $\boldsymbol{\chi}(-2\omega;\omega,\omega)$ for either half. If the supercell itself is centrosymmetric, the value $\boldsymbol{\chi}(-2\omega;\omega,\omega)$ for the full supercell is identically zero. Therefore, the cut function is of paramount importance in order to obtain a finite value for $\boldsymbol{\chi}(-2\omega;\omega,\omega)$ for either side of the slab [28–30]. The cut function can be generalized to one that is capable of obtaining the value of $\boldsymbol{\chi}(-2\omega;\omega,\omega)$ for any part of the slab. The depth within the slab for which $\boldsymbol{\chi}(-2\omega;\omega,\omega)$ is nonzero can thus be obtained. We can also study how $\boldsymbol{\chi}(-2\omega;\omega,\omega)$ goes to zero towards the middle of the slab, where the centrosymmetry of the material is restored [31]. Therefore, for the surface of any centrosymmetric material, we can find the thickness of the layer where $\boldsymbol{\chi}(-2\omega;\omega,\omega)$ is finite.

Based on this approach for the calculation of $\boldsymbol{\chi}(-2\omega;\omega,\omega)$, in this paper we develop a model for the SH radiation from the surface of a centrosymmetric material. We call this model the three-layer model, which considers that the SH conversion takes place in a thin layer just below the surface of the material that lies under the vacuum region and above the bulk

*bms@cio.mx

of the material. Of course, one can replace the vacuum region with any medium as long as it is not SH active; however, most of the experimental setups for measuring the SH radiation take place in vacuum or air. It is the three-layer model that allows us to integrate the effects of multiple reflections, for both the SH and fundamental fields, into the SSHG yield. As mentioned before, the inclusion of these effects is necessary to accurately model the SSHG radiation, and as far as we know, has not been treated before in rigorous detail. Our model considers dielectric materials of any linear reflectance, in contrast with Ref. [18], which assumes a small linear reflectance for their results.

We develop the model and derive general expressions for the SH radiation for the commonly used polarization combinations of the incoming and outgoing electric fields. We particularize the results for the (111), (110), and (001) crystalline surfaces of centrosymmetric materials. As an example, we present results for the SH yield of the Si(111)(1 × 1):H surface, and compare with the experimental results from Ref. [32], showing that the multiple reflections of the three-layer model improve the similarity with the experimental spectra; in particular, we can contrast with recently published results for the same surface [30]. We also present theoretical SSHG predictions for a Si(001)(2 × 1) surface reconstruction. We note that our treatment is strictly valid within the dipole approximation, and we assume that the bulk quadrupolar SHG response is negligible compared to the dipolar contribution, as reported in the experimental works of Refs. [8,20,33–36].

This paper is organized as follows. In Sec. II, we present the relevant equations and theory that describe the SSHG yield; in Secs. II A and II B we present the details for including multiple reflections for both the SH radiation and fundamental fields, respectively. In Sec. III, we present the explicit expressions for each combination of input and output polarizations for the (111), (110), and (001) surfaces. We present our calculated results against the experimental data for the Si(111)(1 × 1):H surface in Sec. IV, and in Sec. V we show the predictions for the Si(001)(2 × 1) surface. Finally, we list our conclusions and final remarks in Sec. VI.

II. THE THREE-LAYER MODEL FOR THE SSHG YIELD

In this section, we will derive the formulas required for the calculation of the SSHG yield, defined by

$$\mathcal{R}(\omega) = \frac{I(2\omega)}{I^2(\omega)}, \tag{1}$$

with the intensity given by [37,38]

$$I(\omega) = \begin{cases} \frac{c}{2\pi} n(\omega)|E(\omega)|^2 & \text{(CGS units)}, \\ 2\epsilon_0 c\, n(\omega)|E(\omega)|^2 & \text{(MKS units)}, \end{cases} \tag{2}$$

where $n(\omega) = [\epsilon(\omega)]^{1/2}$ is the index of refraction with $\epsilon(\omega)$ as the dielectric function, ϵ_0 is the vacuum permittivity, and c is the speed of light in vacuum.

There are several ways to calculate $\mathcal{R}$, one of which is the procedure followed by Cini [22]. This approach calculates the nonlinear susceptibility, and at the same, time the radiated fields; however, we present an alternative derivation based on the work of Mizrahi and Sipe [21], since the derivation of the three-layer model is straightforward. In this scheme, the surface is represented by three regions or layers. The first layer is the vacuum region (denoted by v) with a dielectric function $\epsilon_v(\omega) = 1$, from where the fundamental electric field $\mathbf{E}_v(\omega)$ impinges on the material. The second layer is a thin layer (denoted by ℓ) of thickness d characterized by a dielectric function $\epsilon_\ell(\omega)$; it is in this layer where the SHG takes place. The third layer is the bulk region denoted by b and characterized by $\epsilon_b(\omega)$. Both the vacuum and bulk layers are semi-infinite (see Fig. 1).

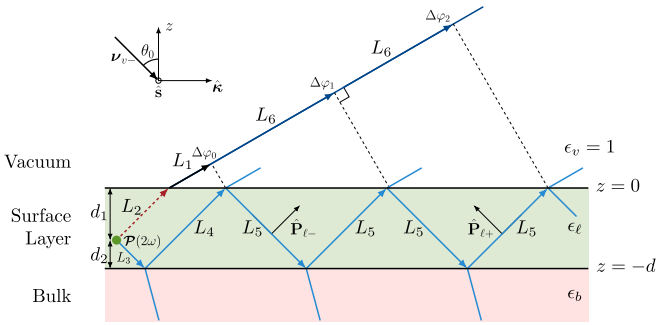

FIG. 1. Sketch of the three-layer model for SHG. The vacuum region (v) is on top with $\epsilon_v = 1$; the layer ℓ of thickness $d = d_1 + d_2$ is characterized by $\epsilon_\ell(\omega)$, and it is where the SH polarization sheet $\mathcal{P}_\ell(2\omega)$ is located at $z_\ell = d_1$. The bulk b is described by $\epsilon_b(\omega)$. The arrows point along the direction of propagation, and the p-polarization unit vector, $\hat{\mathbf{P}}_{\ell-(+)}$, along the downward (upward) direction is denoted with a thick arrow. The s-polarization unit vector $\hat{\mathbf{s}}$ points out of the page. The fundamental field $\mathbf{E}_v(\omega)$ is incident from the vacuum side along the $\hat{\boldsymbol{\kappa}}z$ plane, with θ_0 being its angle of incidence and $\boldsymbol{\nu}_{v-}$ its wave vector. $\Delta\varphi_i$ denotes the phase difference between the multiple reflected beams and the first layer-vacuum transmitted beam, denoted by the dashed red arrow (of length L_2) followed by the solid black arrow (of length L_1). The dotted lines in the vacuum region are perpendicular to the beam extended from the solid black arrow (denoted by solid dark blue arrows of length L_6).

To model the electromagnetic response of the three-layer model, we follow Ref. [21] and assume a polarization sheet of the form

$$\mathbf{P}(\mathbf{r},t) = \mathcal{P} e^{i\hat{\boldsymbol{\kappa}}\cdot\mathbf{R}} e^{-i\omega t} \delta(z - z_\beta) + \text{c.c.}, \tag{3}$$

where $\mathbf{R} = (x, y)$, $\hat{\boldsymbol{\kappa}}$ is the component of the wave vector $\boldsymbol{\nu}_\beta$ parallel to the surface, z_β is the position of the sheet within medium β, and $\mathcal{P}$ is the position-independent polarization. Reference [39] demonstrates that the solution of the Maxwell equations for the radiated fields $E_{\beta,p\pm}$ and $E_{\beta,s}$ with $\mathbf{P}(\mathbf{r},t)$ as a source at points $z \neq 0$ can be written as

$$(E_{\beta,p\pm}, E_{\beta,s}) = \left(\frac{\gamma i \tilde{\omega}^2}{\tilde{w}_\beta} \hat{\mathbf{p}}_{\beta\pm} \cdot \mathcal{P}, \frac{\gamma i \tilde{\omega}^2}{\tilde{w}_\beta} \hat{\mathbf{s}} \cdot \mathcal{P} \right), \tag{4}$$

where $\gamma = 2\pi$ in CGS units or $\gamma = 1/2\epsilon_0$ in MKS units, and $\tilde{\omega} = \omega/c$. Also, $\hat{\mathbf{s}}$ and $\hat{\mathbf{p}}_{\beta\pm}$ are the unit vectors for the s and p polarizations of the radiated field, respectively. The $\pm$ refers to upward (+) or downward (−) direction of propagation within medium β, as shown in Fig. 1. Also, $\tilde{w}_\beta(\omega) = \tilde{\omega} w_\beta$, where

$$\hat{\mathbf{p}}_{\beta\pm}(\omega) = \frac{\kappa(\omega)\hat{\mathbf{z}} \mp \tilde{w}_\beta(\omega)\hat{\boldsymbol{\kappa}}}{\tilde{\omega} n_\beta(\omega)} = \frac{\sin\theta_0 \hat{\mathbf{z}} \mp w_\beta(\omega)\hat{\boldsymbol{\kappa}}}{n_\beta(\omega)}, \tag{5}$$

with

$$w_\beta(\omega) = [\epsilon_\beta(\omega) - \sin^2\theta_0]^{1/2}, \tag{6}$$

where θ_0 is the angle of incidence of $\mathbf{E}_v(\omega)$, $\kappa(\omega) = |\hat{\boldsymbol{\kappa}}| = \tilde{\omega}\sin\theta_0$, $n_\beta(\omega) = [\epsilon_\beta(\omega)]^{1/2}$ is the index of refraction of medium β, and z is the direction perpendicular to the surface that points towards vacuum. If we consider the plane of incidence along the $\hat{\boldsymbol{\kappa}}z$ plane, then

$$\hat{\boldsymbol{\kappa}} = \cos\phi\hat{\mathbf{x}} + \sin\phi\hat{\mathbf{y}} \tag{7}$$

and

$$\hat{\mathbf{s}} = -\sin\phi\hat{\mathbf{x}} + \cos\phi\hat{\mathbf{y}}, \tag{8}$$

where ϕ is the azimuthal angle with respect to the x axis.

In the three-layer model, the nonlinear polarization responsible for the SHG is immersed in the thin layer ($\beta = \ell$), and is given by

$$\mathcal{P}^{\mathrm{a}}_\ell(2\omega) = \begin{cases} \chi^{\mathrm{abc}}_{\mathrm{surface}}(-2\omega;\omega,\omega)E^{\mathrm{b}}(\omega)E^{\mathrm{c}}(\omega) & \text{(CGS)}, \\ \epsilon_0\chi^{\mathrm{abc}}_{\mathrm{surface}}(-2\omega;\omega,\omega)E^{\mathrm{b}}(\omega)E^{\mathrm{c}}(\omega) & \text{(MKS)}, \end{cases} \tag{9}$$

where $\boldsymbol{\chi}_{\mathrm{surface}}(-2\omega;\omega,\omega)$ is the dipolar surface nonlinear susceptibility tensor, and the Cartesian superscripts a, b, and c are summed over if repeated. Also, $\chi^{\mathrm{abc}}(-2\omega;\omega,\omega) = \chi^{\mathrm{acb}}(-2\omega;\omega,\omega)$ due to the intrinsic permutation symmetry, since SHG is degenerate in $E^{\mathrm{b}}(\omega)$ and $E^{\mathrm{c}}(\omega)$. As in Ref. [21], we consider the polarization sheet [Eq. (3)] to be oscillating at some frequency ω in order to properly express Eqs. (4)–(8). However, in the following, we find it convenient to use ω exclusively to denote the fundamental frequency and $\hat{\boldsymbol{\kappa}}$ to denote the component of the incident wave vector parallel to the surface. The generated nonlinear polarization is oscillating at $\Omega = 2\omega$, and will be characterized by a wave vector parallel to the surface $\mathbf{K} = 2\boldsymbol{\kappa}$. We can carry over Eqs. (3)–(8) simply by replacing the lowercase symbols $(\omega,\tilde{\omega},\boldsymbol{\kappa},n_\beta,\tilde{w}_\beta,w_\beta,\hat{\mathbf{p}}_{\beta\pm},\hat{\mathbf{s}})$ with uppercase symbols $(\Omega,\tilde{\Omega},\mathbf{K},N_\beta,\tilde{W}_\beta,W_\beta,\hat{\mathbf{P}}_{\beta\pm},\hat{\mathbf{S}})$, all evaluated at 2ω. Of course, we always have that $\hat{\mathbf{S}} = \hat{\mathbf{s}}$.

From Fig. 1, we observe the propagation of the SH field as it is refracted at the layer-vacuum interface (ℓv), and reflected multiple times from the layer-bulk (ℓb) and layer-vacuum (ℓv) interfaces. Thus, we can define

$$\mathbf{T}^{\ell v} = \hat{\mathbf{s}}T^{\ell v}_s\hat{\mathbf{s}} + \hat{\mathbf{P}}_{v+}T^{\ell v}_p\hat{\mathbf{P}}_{\ell+} \tag{10}$$

as the transmission tensor for the ℓv interface,

$$\mathbf{R}^{\ell b} = \hat{\mathbf{s}}R^{\ell b}_s\hat{\mathbf{s}} + \hat{\mathbf{P}}_{\ell+}R^{\ell b}_p\hat{\mathbf{P}}_{\ell-} \tag{11}$$

as the reflection tensor for the ℓb interface, and

$$\mathbf{R}^{\ell v} = \hat{\mathbf{s}}R^{\ell v}_s\hat{\mathbf{s}} + \hat{\mathbf{P}}_{\ell-}R^{\ell v}_p\hat{\mathbf{P}}_{\ell+} \tag{12}$$

as the reflection tensor for the ℓv interface. The Fresnel factors in uppercase letters, $T^{ij}_{s,p}$ and $R^{ij}_{s,p}$, are evaluated at 2ω from the following well-known formulas [40]:

$$t^{ij}_s(\omega) = \frac{2w_i(\omega)}{w_i(\omega) + w_j(\omega)},$$

$$t^{ij}_p(\omega) = \frac{2w_i(\omega)\sqrt{\epsilon_i(\omega)\epsilon_j(\omega)}}{w_i(\omega)\epsilon_j(\omega) + w_j(\omega)\epsilon_i(\omega)},$$

$$r^{ij}_s(\omega) = \frac{w_i(\omega) - w_j(\omega)}{w_i(\omega) + w_j(\omega)},$$

$$r^{ij}_p(\omega) = \frac{w_i(\omega)\epsilon_j(\omega) - w_j\epsilon_i(\omega)}{w_i(\omega)\epsilon_j(\omega) + w_j(\omega)\epsilon_i(\omega)}. \tag{13}$$

With these expressions, we easily derive the following useful relations,

$$1 + r^{\ell b}_s = t^{\ell b}_s, \quad 1 + r^{\ell b}_p = \frac{n_b}{n_\ell}t^{\ell b}_p,$$

$$1 - r^{\ell b}_p = \frac{n_\ell}{n_b}\frac{w_b}{w_\ell}t^{\ell b}_p, \quad t^{\ell v}_p = \frac{w_\ell}{w_v}t^{v\ell}_p,$$

$$t^{\ell v}_s = \frac{w_\ell}{w_v}t^{v\ell}_s. \tag{14}$$

A. Multiple SHG reflections

The SH field $\mathbf{E}(2\omega)$ generated by the SH polarization $\boldsymbol{\mathcal{P}}_\ell(2\omega)$ will radiate directly into the vacuum and bulk, where it will be reflected back into the thin layer at the layer-bulk interface; this beam will be transmitted and reflected multiple times, as shown in Fig. 1. As the two beams propagate, a phase difference will develop between them according to

$$\begin{aligned}\Delta\varphi_m &= \tilde{\Omega}([L_3 + L_4 + 2mL_5]N_\ell \\ &\quad - [L_2N_\ell + (L_1 + mL_6)N_v]) \\ &= \delta_0 + m\delta, \quad m = 0,1,2,\ldots,\end{aligned} \tag{15}$$

where

$$\delta_0 = 8\pi\left(\frac{d_2}{\lambda_0}\right)W_\ell \tag{16}$$

and

$$\delta = 8\pi\left(\frac{d}{\lambda_0}\right)W_\ell, \tag{17}$$

where λ_0 is the wavelength of the fundamental field in vacuum, W_ℓ is established in Eq. (6), d is the thickness of layer ℓ, and d_2 is the distance between $\boldsymbol{\mathcal{P}}_\ell(2\omega)$ and the ℓb interface (see Fig. 1). We see that δ_0 is the phase difference of the first and second transmitted beams, and $m\delta$ that of the first and third ($m = 1$), first and fourth ($m = 2$), and so on. Note that the thickness d of the layer ℓ enters through the phase δ, and the position d_2 of the nonlinear polarization $\mathbf{P}(\mathbf{r},t)$ [Eq. (3)] enters through δ_0. In particular, d_2 could be used as a variable to study the effects of multiple reflections on the SSHG yield $\mathcal{R}(2\omega)$.

To take into account the multiple reflections of the generated SH field in the layer ℓ, we proceed as follows. We include the algebra for the p-polarized SH field, but the s-polarized field can be worked out following the same steps. The p-polarized $\mathbf{E}_{\ell,p}(2\omega)$ field that is reflected multiple times is given by

$$\begin{aligned}\mathbf{E}_{\ell,p}(2\omega) &= E_{\ell,p+}(2\omega)\mathbf{T}^{\ell v}\cdot\hat{\mathbf{P}}_{\ell+} + E_{\ell,p-}(2\omega)\mathbf{T}^{\ell v}\cdot\mathbf{R}^{\ell b} \\ &\quad\cdot\hat{\mathbf{P}}_{\ell-}e^{i\Delta\varphi_0} + E_{\ell,p-}(2\omega)\mathbf{T}^{\ell v}\cdot\mathbf{R}^{\ell b}\cdot\mathbf{R}^{\ell v}\cdot\mathbf{R}^{\ell b} \\ &\quad\cdot\hat{\mathbf{P}}_{\ell-}e^{i\Delta\varphi_1} + E_{\ell,p-}(2\omega)\mathbf{T}^{\ell v}\cdot\mathbf{R}^{\ell b}\cdot\mathbf{R}^{\ell v}\cdot\mathbf{R}^{\ell b} \\ &\quad\cdot\mathbf{R}^{\ell v}\cdot\mathbf{R}^{\ell b}\cdot\hat{\mathbf{P}}_{\ell-}e^{i\Delta\varphi_2} + \cdots \\ &= E_{\ell,p+}(2\omega)\mathbf{T}^{\ell v}\cdot\hat{\mathbf{P}}_{\ell+} + E_{\ell,p-}(2\omega)\mathbf{T}^{\ell v} \\ &\quad\cdot\sum_{m=0}^{\infty}(\mathbf{R}^{\ell b}\cdot\mathbf{R}^{\ell v}e^{i\delta})^m\cdot\mathbf{R}^{\ell b}\cdot\hat{\mathbf{P}}_{\ell-}e^{i\delta_0}.\end{aligned} \tag{18}$$

From Eqs. (10)–(12), it is easy to show that

$$\mathbf{T}^{\ell v}\cdot(\mathbf{R}^{\ell b}\cdot\mathbf{R}^{\ell v})^m\cdot\mathbf{R}^{\ell b} = \hat{\mathbf{s}}T_s^{\ell v}\left(R_s^{\ell b}R_s^{\ell v}\right)^m R_s^{\ell b}\hat{\mathbf{s}} + \hat{\mathbf{P}}_{v+}T_p^{\ell v}\left(R_p^{\ell b}R_p^{\ell v}\right)^m R_p^{\ell b}\hat{\mathbf{P}}_{\ell-},$$

then,

$$\mathbf{E}_{\ell,p}(2\omega) = \hat{\mathbf{P}}_{\ell+}T_p^{\ell v}\left(E_{\ell,p+}(2\omega) + \frac{R_p^{\ell b}e^{i\delta_0}}{1+R_p^{v\ell}R_p^{\ell b}e^{i\delta}}E_{\ell,p-}(2\omega)\right),$$

where we used $R_{s,p}^{ij} = -R_{s,p}^{ji}$. Using Eqs. (4) and (14), we can readily write

$$\mathbf{E}_{\ell,p}(2\omega) = \frac{\gamma i\tilde{\Omega}}{W_\ell}\mathbf{H}_\ell\cdot\boldsymbol{\mathcal{P}}_\ell(2\omega), \tag{19}$$

where

$$\mathbf{H}_\ell = \frac{W_\ell}{W_v}\left[\hat{\mathbf{s}}\,T_s^{v\ell}\left(1+R_s^M\right)\hat{\mathbf{s}} + \hat{\mathbf{P}}_{v+}T_p^{v\ell}\left(\hat{\mathbf{P}}_{\ell+}+R_p^M\hat{\mathbf{P}}_{\ell-}\right)\right], \tag{20}$$

and

$$R_i^M \equiv \frac{R_i^{\ell b}e^{i\delta_0}}{1+R_i^{v\ell}R_i^{\ell b}e^{i\delta}}, \quad i=s,p, \tag{21}$$

defines the multiple (M) reflection coefficient. This coefficient depends on the thickness d of layer ℓ, and most importantly, on the position d_2 of $\boldsymbol{\mathcal{P}}_\ell(2\omega)$ within this layer. The final results will depend on both d and d_2. However, using Eq. (16) we can also define an average $\bar{R}_i^M$ as

$$\bar{R}_i^M \equiv \frac{1}{d}\int_0^d \frac{R_i^{\ell b}e^{i(8\pi W_\ell/\lambda_0)x}}{1+R_i^{v\ell}R_i^{\ell b}e^{i\delta}}\,dx = \frac{R_i^{\ell b}e^{i\delta/2}}{1+R_i^{v\ell}R_i^{\ell b}e^{i\delta}}\,\mathrm{sinc}(\delta/2) \tag{22}$$

that only depends on d through the δ term from Eq. (17).

To connect with the work in Ref. [21], where $\boldsymbol{\mathcal{P}}(2\omega)$ is located on top of the vacuum-surface interface, and only the vacuum radiated beam and the first (and only) reflected beam need be considered, we take $\ell = v$ and $d_2 = 0$, then $T^{\ell v} = 1$, $R^{v\ell} = 0$, and $\delta_0 = 0$, with which $R_i^M = R_i^{vb}$. Thus, Eq. (20) coincides with Eq. (3.8) of Ref. [21].

B. Multiple reflections for the linear field

For a more complete formulation, we must also consider the multiple reflections of the fundamental field $\mathbf{E}_\ell(\omega)$ inside the thin ℓ layer. In Fig. 2, we present the situation where $\mathbf{E}_v(\omega)$ impinges from the vacuum side with an angle of incidence θ_0. As the first transmitted beam is reflected multiple times from the ℓb and the $v\ell$ interfaces, it accumulates a phase difference of $n\varphi$ ($n = 1,2,3,\ldots$), where φ is given by

$$\varphi = \frac{\omega}{c}(2L_1n_\ell - L_2n_v) = 4\pi\left(\frac{d}{\lambda_0}\right)w_\ell, \tag{23}$$

where $n_v = 1$. Besides the equivalent of Eqs. (11) and (12) for ω, we also need

$$\mathbf{t}^{v\ell} = \hat{\mathbf{s}}t_s^{v\ell}\hat{\mathbf{s}} + \hat{\mathbf{p}}_{\ell-}t_p^{v\ell}\hat{\mathbf{p}}_{v-} \tag{24}$$

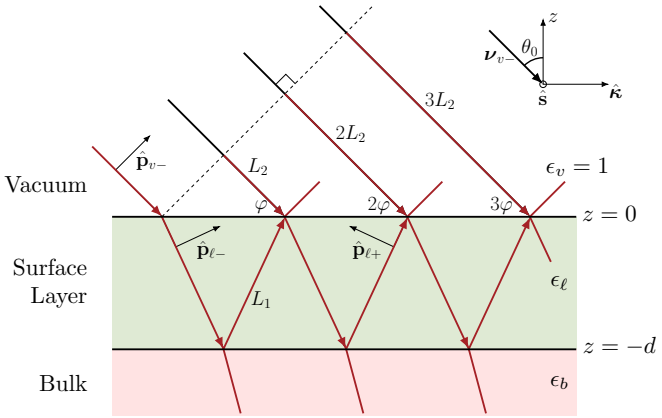

FIG. 2. Sketch for the multiple reflected fundamental field $\mathbf{E}_\ell(\omega)$, which impinges from the vacuum side along the $\hat{\boldsymbol{\kappa}}z$ plane. θ_0 and $\boldsymbol{\nu}_{v-}$ are the angle of incidence and wave vector, respectively. The arrows point along the direction of propagation. The p-polarization unit vectors $\hat{\mathbf{p}}_{\beta\pm}$ point along the downward ($-$) or upward ($+$) directions and are denoted with black arrows, where $\beta = v$ or ℓ. The s-polarization unit vector $\hat{\mathbf{s}}$ points out of the page. $(1,2,3,\ldots)\varphi$ denotes the phase difference for the multiple reflected beams with respect to the incident field, where the dotted line is perpendicular to this beam.

to write

$$\begin{aligned}\mathbf{E}_\ell(\omega) &= E_0[\mathbf{t}^{v\ell} + \mathbf{r}^{\ell b}\cdot\mathbf{t}^{v\ell}e^{i\varphi} + \mathbf{r}^{\ell b}\cdot\mathbf{r}^{\ell v}\cdot\mathbf{r}^{\ell b}\cdot\mathbf{t}^{v\ell}e^{i2\varphi} \\ &\quad + \mathbf{r}^{\ell b}\cdot\mathbf{r}^{\ell v}\cdot\mathbf{r}^{\ell b}\cdot\mathbf{r}^{\ell v}\cdot\mathbf{r}^{\ell b}\cdot\mathbf{t}^{v\ell}e^{i3\varphi} + \cdots]\cdot\hat{\mathbf{e}}^i \\ &= E_0[1 + (1 + \mathbf{r}^{\ell b}\cdot\mathbf{r}^{\ell v}e^{i\varphi} + (\mathbf{r}^{\ell b}\cdot\mathbf{r}^{\ell v})^2e^{i2\varphi} + \cdots) \\ &\quad \cdot\mathbf{r}^{\ell b}e^{i\varphi}]\cdot\mathbf{t}^{v\ell}\cdot\hat{\mathbf{e}}^i \\ &= E_0\left[\hat{\mathbf{s}}t_s^{v\ell}\left(1+r_s^M\right)\hat{\mathbf{s}} + t_p^{v\ell}\left(\hat{\mathbf{p}}_{\ell-}+\hat{\mathbf{p}}_{\ell+}r_p^M\right)\hat{\mathbf{p}}_{v-}\right]\cdot\hat{\mathbf{e}}^i,\end{aligned} \tag{25}$$

where E_0 is the intensity of the fundamental field, and $\hat{\mathbf{e}}^i$ is the unit vector of the incoming polarization, with $i = s,p$, and then, $\hat{\mathbf{e}}^s = \hat{\mathbf{s}}$ and $\hat{\mathbf{e}}^p = \hat{\mathbf{p}}_{v-}$. Also,

$$r_i^M \equiv \frac{r_i^{\ell b}e^{i\varphi}}{1+r_i^{v\ell}r_i^{\ell b}e^{i\varphi}}, \quad i=s,p. \tag{26}$$

r_i^M is defined as the multiple (M) reflection coefficient for the fundamental field. We define $\mathbf{E}_\ell^i(\omega) \equiv E_0\mathbf{e}_\ell^{\omega,i}$ ($i = s,p$), where

$$\mathbf{e}_\ell^{\omega,i} = \left[\hat{\mathbf{s}}t_s^{v\ell}\left(1+r_s^M\right)\hat{\mathbf{s}} + t_p^{v\ell}\left(\hat{\mathbf{p}}_{\ell-}+\hat{\mathbf{p}}_{\ell+}r_p^M\right)\hat{\mathbf{p}}_{v-}\right]\cdot\hat{\mathbf{e}}^i, \tag{27}$$

and using Eq. (5), we obtain that

$$\mathbf{e}_\ell^{\omega,p} = \frac{t_p^{v\ell}}{n_\ell}\left(r_p^{M+}\sin\theta_0\hat{\mathbf{z}} + r_p^{M-}w_\ell\hat{\boldsymbol{\kappa}}\right) \tag{28}$$

for p-input polarization with $\hat{\mathbf{e}}^i = \hat{\mathbf{p}}_{v-}$, and

$$\mathbf{e}_\ell^{\omega,s} = t_s^{v\ell}r_s^{M+}\hat{\mathbf{s}} \tag{29}$$

for s-input polarization with $\hat{\mathbf{e}}^i = \hat{\mathbf{s}}$, where

$$r_i^{M\pm} = 1 \pm r_i^M, \quad i=s,p. \tag{30}$$

C. The SSHG yield

The magnitude of the radiated field is given by $E(2\omega) = \hat{\mathbf{e}}^F \cdot \mathbf{E}_\ell(2\omega)$, where $\hat{\mathbf{e}}^F$ is the unit vector of the final, S or P SH polarization with $F = S, P$, where $\hat{\mathbf{e}}^S = \hat{\mathbf{s}}$ and $\hat{\mathbf{e}}^P = \hat{\mathbf{P}}_{v+}$. We expand the rightmost term in parentheses in Eq. (20) as

$$\hat{\mathbf{P}}_{\ell+} + R_p^M \hat{\mathbf{P}}_{\ell-} = \frac{\sin\theta_0 \hat{\mathbf{z}} - W_\ell \hat{\boldsymbol{\kappa}}}{N_\ell} + R_p^M \frac{\sin\theta_0 \hat{\mathbf{z}} + W_\ell \hat{\boldsymbol{\kappa}}}{N_\ell} = \frac{1}{N_\ell}\left(\sin\theta_0 R_p^{M+} \hat{\mathbf{z}} - W_\ell R_p^{M-} \hat{\boldsymbol{\kappa}}\right),$$

where

$$R_i^{M\pm} \equiv 1 \pm R_i^M, \quad i = s, p. \tag{31}$$

Using Eq. (14), we write Eq. (19) as

$$E(2\omega) = \frac{2\gamma i\omega}{cW_\ell} \hat{\mathbf{e}}^F \cdot \mathbf{H}_\ell \cdot \boldsymbol{\mathcal{P}}_\ell(2\omega) = \frac{2\gamma i\omega}{cW_v} \mathbf{e}_\ell^{2\omega,F} \cdot \boldsymbol{\mathcal{P}}_\ell(2\omega), \tag{32}$$

where

$$\mathbf{e}_\ell^{2\omega,F} = \hat{\mathbf{e}}^F \cdot \left[\hat{\mathbf{s}} T_s^{v\ell} R_s^{M+} \hat{\mathbf{s}} + \hat{\mathbf{P}}_{v+} \frac{T_p^{v\ell}}{N_\ell} \times \left(\sin\theta_0 R_p^{M+} \hat{\mathbf{z}} - W_\ell R_p^{M-} \hat{\boldsymbol{\kappa}}\right)\right]. \tag{33}$$

Replacing $\mathbf{E}_\ell(\omega) \to E_0 \mathbf{e}_\ell^{\omega,i}$ in Eq. (9), we obtain that

$$\boldsymbol{\mathcal{P}}_\ell(2\omega) = \begin{cases} E_0^2\, \boldsymbol{\chi}_{\text{surface}} : \mathbf{e}_\ell^{\omega,i} \mathbf{e}_\ell^{\omega,i} & \text{(CGS units)}, \\ \epsilon_0 E_0^2\, \boldsymbol{\chi}_{\text{surface}} : \mathbf{e}_\ell^{\omega,i} \mathbf{e}_\ell^{\omega,i} & \text{(MKS units)}, \end{cases} \tag{34}$$

where $\mathbf{e}_\ell^{\omega,i}$ is given by Eq. (27), and thus Eq. (32) reduces to ($W_v = \cos\theta_0$)

$$E_\ell(2\omega) = \frac{2\eta i\omega}{c\cos\theta_0} \mathbf{e}_\ell^{2\omega,F} \cdot \boldsymbol{\chi}_{\text{surface}} : \mathbf{e}_\ell^{\omega,i} \mathbf{e}_\ell^{\omega,i}, \tag{35}$$

where $\eta = 2\pi$ in CGS units and $\eta = 1/2$ in MKS units. For ease of notation, we define

$$\Upsilon_{iF} \equiv \mathbf{e}_\ell^{2\omega,F} \cdot \boldsymbol{\chi}_{\text{surface}} : \mathbf{e}_\ell^{\omega,i} \mathbf{e}_\ell^{\omega,i}, \tag{36}$$

where i stands for the incoming polarization of the fundamental electric field given by $\hat{\mathbf{e}}^i$ in Eq. (27), and F for the outgoing polarization of the SH electric field given by $\hat{\mathbf{e}}^F$ in Eq. (33). We purposely omit the full $\boldsymbol{\chi}(-2\omega;\omega,\omega)$ notation, and will do so from this point on.

From Eqs. (1) and (2) we obtain that in CGS units ($\eta = 2\pi$),

$$\begin{aligned} |E(2\omega)|^2 &= |E_0|^4 \frac{16\pi^2\omega^2}{c^2 W_v^2} |\Upsilon_{iF}|^2, \\ \frac{c}{2\pi}|\sqrt{N_v} E(2\omega)|^2 &= \frac{32\pi^3\omega^2}{c^3\cos^2\theta_0} \left|\frac{\sqrt{N_v}}{n_\ell^2} \Upsilon_{iF}\right|^2 \left(\frac{c}{2\pi}|\sqrt{n_\ell} E_0|^2\right)^2, \\ I(2\omega) &= \frac{32\pi^3\omega^2}{c^3\cos^2\theta_0} \left|\frac{\sqrt{N_v}}{n_\ell^2} \Upsilon_{iF}\right|^2 I^2(\omega), \\ \mathcal{R}_{iF}(2\omega) &= \frac{32\pi^3\omega^2}{c^3\cos^2\theta_0} \left|\frac{1}{n_\ell} \Upsilon_{iF}\right|^2, \end{aligned} \tag{37}$$

and in MKS units ($\eta = 1/2$),

$$\begin{aligned} |E(2\omega)|^2 &= |E_0|^4 \frac{\omega^2}{c^2 W_v^2}, \\ 2\epsilon_0 c|\sqrt{N_v} E(2\omega)|^2 &= \frac{2\epsilon_0\omega^2}{c\cos^2\theta_0} \left|\frac{\sqrt{N_v}}{n_\ell^2} \Upsilon_{iF}\right|^2 \times \frac{1}{4\epsilon_0^2 c^2} (2\epsilon_0 c|\sqrt{n_\ell} E_0|^2)^2, \\ I(2\omega) &= \frac{\omega^2}{2\epsilon_0 c^3\cos^2\theta_0} \left|\frac{\sqrt{N_v}}{n_\ell^2} \Upsilon_{iF}\right|^2 I^2(\omega), \\ \mathcal{R}_{iF}(2\omega) &= \frac{\omega^2}{2\epsilon_0 c^3\cos^2\theta_0} \left|\frac{1}{n_\ell} \Upsilon_{iF}\right|^2. \end{aligned} \tag{38}$$

Finally, we condense these results and establish the SSHG yield as

$$\mathcal{R}_{iF}(2\omega) \begin{cases} \frac{32\pi^3\omega^2}{c^3\cos^2\theta_0} \left|\frac{1}{n_\ell} \Upsilon_{iF}\right|^2 & \text{(CGS units)}, \\ \frac{\omega^2}{2\epsilon_0 c^3\cos^2\theta_0} \left|\frac{1}{n_\ell} \Upsilon_{iF}\right|^2 & \text{(MKS units)}, \end{cases} \tag{39}$$

where $N_v = 1$ and $W_v = \cos\theta_0$. We mention that $\boldsymbol{\chi}_{\text{surface}}$ is given in m^2/V in the MKS unit system since it is a surface second-order nonlinear susceptibility. In this system of units, $\mathcal{R}_{iF}$ is in m^2/W.

III. $\mathcal{R}_{iF}$ FOR DIFFERENT POLARIZATION CASES

We now have everything needed to derive explicit expressions for $\mathcal{R}_{iF}$, Eq. (39), for the most commonly used polarizations of incoming and outgoing fields ($iF = pP$, pS, sP, and sS). For this, we must expand Υ_{iF} from Eq. (36) for each case. By substituting Eqs. (7) and (8) into Eq. (33), we obtain

$$\mathbf{e}_\ell^{2\omega,P} = \frac{T_p^{v\ell}}{N_\ell}\left(\sin\theta_0 R_p^{M+} \hat{\mathbf{z}} - W_\ell R_p^{M-} \cos\phi \hat{\mathbf{x}} - W_\ell R_p^{M-} \sin\phi \hat{\mathbf{y}}\right), \tag{40}$$

for P ($\hat{\mathbf{e}}^F = \hat{\mathbf{P}}_{v+}$) outgoing polarization, and

$$\mathbf{e}_\ell^{2\omega,S} = T_s^{v\ell} R_s^{M+}(-\sin\phi \hat{\mathbf{x}} + \cos\phi \hat{\mathbf{y}}), \tag{41}$$

for S ($\hat{\mathbf{e}}^F = \hat{\mathbf{s}}$) outgoing polarization.

Following a similar procedure, we use Eqs. (7) and (8) with Eq. (28), and obtain

$$\begin{aligned} \mathbf{e}_\ell^{\omega,p} \mathbf{e}_\ell^{\omega,p} = \left(\frac{t_p^{v\ell}}{n_\ell}\right)^2 \big[&\left(r_p^{M-}\right)^2 w_\ell^2 \cos^2\phi \hat{\mathbf{x}}\hat{\mathbf{x}} + 2\left(r_p^{M-}\right)^2 w_\ell^2 \times \sin\phi\cos\phi \hat{\mathbf{x}}\hat{\mathbf{y}} + 2 r_p^{M+} r_p^{M-} w_\ell \sin\theta_0 \cos\phi \hat{\mathbf{x}}\hat{\mathbf{z}} \\ &+ \left(r_p^{M-}\right)^2 w_\ell^2 \sin^2\phi \hat{\mathbf{y}}\hat{\mathbf{y}} + 2 r_p^{M+} r_p^{M-} w_\ell \sin\theta_0 \times \sin\phi \hat{\mathbf{y}}\hat{\mathbf{z}} + \left(r_p^{M+}\right)^2 \sin^2\theta_0 \hat{\mathbf{z}}\hat{\mathbf{z}}\big], \end{aligned} \tag{42}$$

for p incoming polarization ($\hat{\mathbf{e}}^i = \hat{\mathbf{p}}_{v-}$), and with Eq. (29),

$$\mathbf{e}_\ell^{\omega,s} \mathbf{e}_\ell^{\omega,s} = \left(t_s^{v\ell} r_s^{M+}\right)^2 (\sin^2\phi \hat{\mathbf{x}}\hat{\mathbf{x}} + \cos^2\phi \hat{\mathbf{y}}\hat{\mathbf{y}} - 2\sin\phi\cos\phi \hat{\mathbf{x}}\hat{\mathbf{y}}), \tag{43}$$

TABLE I. Polarization unit vectors for $\hat{\mathbf{e}}^F$ and $\hat{\mathbf{e}}^i$, and equations describing $\mathbf{e}_\ell^{2\omega,F}$ and $\mathbf{e}_\ell^{\omega,i}\mathbf{e}_\ell^{\omega,i}$ for each polarization case.

Case	$\hat{\mathbf{e}}^F$	$\hat{\mathbf{e}}^i$	$\mathbf{e}_\ell^{2\omega,F}$	$\mathbf{e}_\ell^{\omega,i}\mathbf{e}_\ell^{\omega,i}$
$\mathcal{R}_{pP}$	$\hat{\mathbf{P}}_{v+}$	$\hat{\mathbf{p}}_{v-}$	Eq. (40)	Eq. (42)
$\mathcal{R}_{pS}$	$\hat{\mathbf{S}}$	$\hat{\mathbf{p}}_{v-}$	Eq. (41)	Eq. (42)
$\mathcal{R}_{sP}$	$\hat{\mathbf{P}}_{v+}$	$\hat{\mathbf{s}}$	Eq. (40)	Eq. (43)
$\mathcal{R}_{sS}$	$\hat{\mathbf{S}}$	$\hat{\mathbf{s}}$	Eq. (41)	Eq. (43)

for s incoming polarization ($\hat{\mathbf{e}}^i = \hat{\mathbf{s}}$). We have summarized the combination of equations needed to derive the expressions for all four polarization cases of $\mathcal{R}_{iF}$ in Table I. In the following subsections we will derive the explicit expressions for Υ_{iF} for the most general case where the surface has no symmetry. We will then develop these expressions for particular cases of the most commonly investigated surfaces, the (111), (001), and (110) crystallographic faces. For ease of notation, we split Υ_{iF} as

$$\Upsilon_{iF} = \Gamma_{iF}\, r_{iF}, \tag{44}$$

and omit the "surface" subscript for the χ^{abc} components. A full, step-by-step derivation for all of these expressions can be found in Ref. [41], with and without the effects of multiple reflections.

Many expressions can be greatly simplified by introducing a matrix representation for $\boldsymbol{\chi}$. Disregarding all symmetry relations, we have

$$\boldsymbol{\chi} = \left(\begin{array}{ccc|ccc} \chi^{xxx} & \chi^{xyy} & \chi^{xzz} & \chi^{xyz} & \chi^{xxz} & \chi^{xxy} \\ \chi^{yxx} & \chi^{yyy} & \chi^{yzz} & \chi^{yyz} & \chi^{yxz} & \chi^{yxy} \\ \chi^{zxx} & \chi^{zyy} & \chi^{zzz} & \chi^{zyz} & \chi^{zxz} & \chi^{zxy} \end{array}\right), \tag{45}$$

where all 18 independent components are accounted for, recalling that $\chi^{\mathrm{abc}} = \chi^{\mathrm{acb}}$ for SHG. Notice that the left-hand block contains the components of χ^{abc} where $b = c$, and the right hand block those where $b \neq c$. As mentioned above, we are interested in the (111), (110), and (001) crystallographic faces, that belong to the C_{3v}, C_{2v}, and C_{4v} symmetry groups, respectively. For the (111) surface, we choose the x and y axes along the $[11\bar{2}]$ and $[1\bar{1}]0$ directions, respectively. For the (110) and (001), we consider the y axis perpendicular to the plane of symmetry [20]. These are represented in matrix form as

$$\boldsymbol{\chi}^{(111)} = \left(\begin{array}{ccc|ccc} \chi^{xxx} & -\chi^{xxx} & 0 & 0 & \chi^{xxz} & 0 \\ 0 & 0 & 0 & \chi^{xxz} & 0 & -\chi^{xxx} \\ \chi^{zxx} & \chi^{zxx} & \chi^{zzz} & 0 & 0 & 0 \end{array}\right), \tag{46}$$

$$\boldsymbol{\chi}^{(110)} = \left(\begin{array}{ccc|ccc} 0 & 0 & 0 & 0 & \chi^{xxz} & 0 \\ 0 & 0 & 0 & \chi^{yyz} & 0 & 0 \\ \chi^{zxx} & \chi^{zyy} & \chi^{zzz} & 0 & 0 & 0 \end{array}\right), \tag{47}$$

and

$$\boldsymbol{\chi}^{(001)} = \left(\begin{array}{ccc|ccc} 0 & 0 & 0 & 0 & \chi^{xxz} & 0 \\ 0 & 0 & 0 & \chi^{xxz} & 0 & 0 \\ \chi^{zxx} & \chi^{zxx} & \chi^{zzz} & 0 & 0 & 0 \end{array}\right). \tag{48}$$

In general, $\boldsymbol{\chi}^{(111)} \neq \boldsymbol{\chi}^{(110)} \neq \boldsymbol{\chi}^{(001)}$.

A. $\mathcal{R}_{pP}$ (p in, P out)

Per Table I, $\mathcal{R}_{pP}$ requires Eqs. (40) and (42). After some algebra, we obtain that

$$\Gamma_{pP} = \frac{T_p^{v\ell}}{N_\ell}\left(\frac{t_p^{v\ell}}{n_\ell}\right)^2 \tag{49}$$

and

$$r_{pP} = \begin{pmatrix} -R_p^{M-} W_\ell \cos\phi \\ -R_p^{M-} W_\ell \sin\phi \\ +R_p^{M+} \sin\theta_0 \end{pmatrix} \circ \boldsymbol{\chi} \cdot \begin{pmatrix} \left(r_p^{M-}\right)^2 w_\ell^2 \cos^2\phi \\ \left(r_p^{M-}\right)^2 w_\ell^2 \sin^2\phi \\ \left(r_p^{M+}\right)^2 \sin^2\theta_0 \\ 2 r_p^{M+} r_p^{M-} w_\ell \sin\theta_0 \sin\phi \\ 2 r_p^{M+} r_p^{M-} w_\ell \sin\theta_0 \cos\phi \\ 2\left(r_p^{M-}\right)^2 w_\ell^2 \sin\phi\cos\phi \end{pmatrix}, \tag{50}$$

where all 18 independent components of $\boldsymbol{\chi}$ can contribute to $\mathcal{R}_{pP}$. The "$\circ$" symbol is the Hadamard (piecewise) matrix product. For the (111) surface, we substitute Eq. (46) in Eq. (50) in lieu of $\boldsymbol{\chi}$ to obtain

$$\begin{aligned} r_{pP}^{(111)} = {} & R_p^{M+} \sin\theta_0 \left[\left(r_p^{M+}\right)^2 \sin^2\theta_0 \chi^{zzz} + \left(r_p^{M-}\right)^2 w_\ell^2 \chi^{zxx}\right] \\ & - R_p^{M-} w_\ell W_\ell \left[2 r_p^{M+} r_p^{M-} \sin\theta_0 \chi^{xxz} \right. \\ & \left. + \left(r_p^{M-}\right)^2 w_\ell \chi^{xxx} \cos 3\phi\right], \end{aligned} \tag{51}$$

where the threefold azimuthal symmetry of the SHG signal that is typical of the C_{3v} symmetry group is seen in the 3ϕ argument of the cosine function. For the (110) surface, we substitute Eq. (47) in Eq. (50) to obtain

$$\begin{aligned} r_{pP}^{(110)} = {} & R_p^{M+} \sin\theta_0 \left[\left(r_p^{M+}\right)^2 \sin^2\theta_0 \chi^{zzz} + \left(r_p^{M-}\right)^2 w_\ell^2 \right. \\ & \left. \times \left(\frac{\chi^{zyy} + \chi^{zxx}}{2} + \frac{\chi^{zyy} - \chi^{zxx}}{2}\cos 2\phi\right)\right] \\ & - 2 R_p^{M-} r_p^{M+} r_p^{M-} w_\ell W_\ell \sin\theta_0 \left(\frac{\chi^{yyz} + \chi^{xxz}}{2} \right. \\ & \left. + \frac{\chi^{yyz} - \chi^{xxz}}{2}\cos 2\phi\right). \end{aligned} \tag{52}$$

The twofold azimuthal symmetry of the SHG signal that is typical of the C_{2v} symmetry group is seen in the 2ϕ argument of the cosine function. Lastly, for the (001) surface we simply make $\chi^{zxx} = \chi^{zyy}$ and $\chi^{xxz} = \chi^{yyz}$ [see Eqs. (47) and (48)], and the previous expression reduces to

$$\begin{aligned} r_{pP}^{(001)} = {} & R_p^{M+} \sin\theta_0 \left[\left(r_p^{M+}\right)^2 \sin^2\theta_0 \chi^{zzz} + \left(r_p^{M-}\right)^2 w_\ell^2 \chi^{zxx}\right] \\ & - 2 R_p^{M-} r_p^{M+} r_p^{M-} w_\ell W_\ell \sin\theta_0 \chi^{xxz}. \end{aligned} \tag{53}$$

This time, the azimuthal 4ϕ symmetry for the C_{4v} group of the (001) surface is absent in this expression since this contribution is only related to the bulk nonlinear quadrupolar SH term [20], which we neglect in this work.

B. $\mathcal{R}_{sP}$ (*s* in, *P* out)

Per Table I, $\mathcal{R}_{sP}$ requires Eqs. (40) and (43). After some algebra, we obtain that

$$\Gamma_{sP} = \frac{T_p^{v\ell}}{N_\ell}\left(t_s^{v\ell} r_s^{M+}\right)^2 \tag{54}$$

and

$$r_{sP} = \begin{pmatrix} -R_p^{M-} W_\ell \cos\phi \\ -R_p^{M-} W_\ell \sin\phi \\ +R_p^{M+} \sin\theta_0 \end{pmatrix} \circ \boldsymbol{\chi} \cdot \begin{pmatrix} \sin^2\phi \\ \cos^2\phi \\ 0 \\ 0 \\ 0 \\ -2\sin\phi\cos\phi \end{pmatrix}. \tag{55}$$

In this case, 9 out of the 18 components of $\boldsymbol{\chi}$ can contribute to $\mathcal{R}_{sP}$. This is because there is no $E_v^z(\omega)$ component, as the incoming polarization is *s*. As before, we substitute Eqs. (46), (47), and (48) in Eq. (55) to obtain

$$r_{sP}^{(111)} = R_p^{M+} \sin\theta_0 \chi^{zxx} + R_p^{M-} W_\ell \chi^{xxx} \cos 3\phi \tag{56}$$

for the (111) surface,

$$r_{sP}^{(110)} = R_p^{M+} \sin\theta_0 \left(\frac{\chi^{zxx} + \chi^{zyy}}{2} + \frac{\chi^{zyy} - \chi^{zxx}}{2} \cos 2\phi \right) \tag{57}$$

for the (110) surface, and

$$r_{sP}^{(001)} = R_p^{M+} \sin\theta_0 \chi^{zxx} \tag{58}$$

for the (001) surface.

C. $\mathcal{R}_{pS}$ (*p* in, *S* out)

Per Table I, $\mathcal{R}_{pS}$ requires Eqs. (41) and (42). After some algebra, we obtain that

$$\Gamma_{pS} = T_s^{v\ell} R_s^{M+} \left(\frac{t_p^{v\ell}}{n_\ell} \right)^2 \tag{59}$$

and

$$r_{pS} = \begin{pmatrix} -\sin\phi \\ \cos\phi \\ 0 \end{pmatrix} \circ \boldsymbol{\chi} \cdot \begin{pmatrix} \left(r_p^{M-}\right)^2 w_\ell^2 \cos^2\phi \\ \left(r_p^{M-}\right)^2 w_\ell^2 \sin^2\phi \\ \left(r_p^{M+}\right)^2 \sin^2\theta_0 \\ 2 r_p^{M+} r_p^{M-} w_\ell \sin\theta_0 \sin\phi \\ 2 r_p^{M+} r_p^{M-} w_\ell \sin\theta_0 \cos\phi \\ 2\left(r_p^{M-}\right)^2 w_\ell^2 \sin\phi\cos\phi \end{pmatrix}. \tag{60}$$

In this case, 12 out of the 18 components of $\boldsymbol{\chi}$ can contribute to $\mathcal{R}_{pS}$. This is because there is no $\mathcal{P}_\ell^z(2\omega)$ component, as the outgoing polarization is *S*. As before, we substitute Eqs. (46), (47), and (48) in Eq. (60) to obtain

$$r_{pS}^{(111)} = -\left(r_p^{M-}\right)^2 w_\ell^2 \chi^{xxx} \sin 3\phi \tag{61}$$

for the (111) surface,

$$r_{pS}^{(110)} = r_p^{M+} r_p^{M-} w_\ell \sin\theta_0 (\chi^{yyz} - \chi^{xxz}) \sin 2\phi \tag{62}$$

for the (110) surface, and finally,

$$r_{pS}^{(001)} = 0 \tag{63}$$

for the (001) surface, where the zero value is only surface related, as we neglect the bulk nonlinear quadrupolar contribution [20].

D. $\mathcal{R}_{sS}$ (*s* in, *S* out)

Per Table I, $\mathcal{R}_{sS}$ requires Eqs. (41) and (43). After some algebra, we obtain that

$$\Gamma_{sS} = T_s^{v\ell} R_s^{M+} \left(t_s^{v\ell} r_s^{M+}\right)^2 \tag{64}$$

and

$$r_{sS} = \begin{pmatrix} -\sin\phi \\ \cos\phi \\ 0 \end{pmatrix} \circ \boldsymbol{\chi} \cdot \begin{pmatrix} \sin^2\phi \\ \cos^2\phi \\ 0 \\ 0 \\ 0 \\ -2\sin\phi\cos\phi \end{pmatrix}. \tag{65}$$

In this case, only 6 out of the 18 components of $\boldsymbol{\chi}$ can contribute to $\mathcal{R}_{sS}$. This is because there is neither an $E_v^z(\omega)$ component as the incoming polarization is *s*, nor a $\mathcal{P}_\ell^z(2\omega)$ component as the outgoing polarization is *S*. As before, we substitute Eqs. (46), (47), and (48) in Eq. (65) to obtain

$$r_{sS}^{(111)} = \chi^{xxx} \sin 3\phi \tag{66}$$

for the (111) surface, and

$$r_{sS}^{(110)} = 0 \tag{67}$$

and

$$r_{sS}^{(001)} = 0 \tag{68}$$

for the (110) and (001) surfaces, respectively, both being zero as the bulk nonlinear quadrupolar contribution is not considered here [20].

IV. SSHG OF THE Si(111)(1 × 1):H SURFACE

We consider that the Si(111)(1 × 1):H surface is an excellent case to test the three-layer model and study the effects that multiple reflections have on the SSHG yield. This surface is well characterized experimentally [32,42,43], and there has been success in reproducing these experimental results using the three-layer model without multiple reflections [30]. The details of the *ab initio* calculation of χ^{abc} are discussed in Ref. [30]. We mention that we apply a scissors shift of 0.7 eV to the theoretical spectra. In a first approximation, this includes the effects of the electronic many-body interactions within the independent-particle approach for our *ab initio* calculation. This 0.7 eV value allows the SH resonant peaks to acquire their corresponding energy positions, and is obtained from a G_0W_0 calculation [30,44]. As mentioned in Sec. I, we are interested in finding the thickness of the layer ℓ where $\chi^{abc} \neq 0$. For this surface, we found well-converged results for a thickness of ~ 5 nm, which is equivalent to 24 atomic sheets of Si along

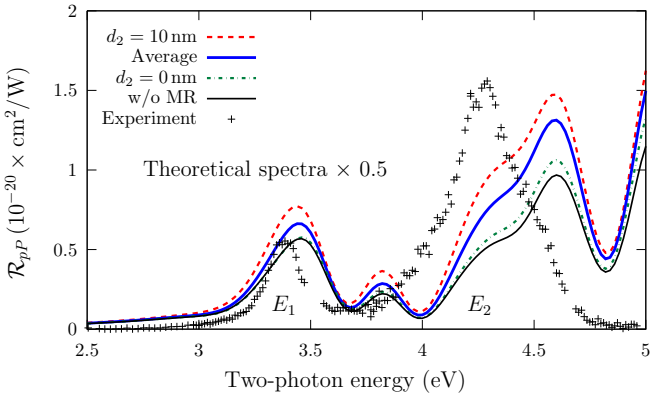

FIG. 3. Comparison of $\mathcal{R}_{pP}$ between the three-layer model with the effects of multiple reflections for two different values of d_2, using the average value $\bar{R}_P^M$ of Eq. (22), the three-layer model without the effects of multiple reflections, and the experimental data from Ref. [32]. All curves that include multiple reflections consider the thickness of the layer ℓ as $d = 10$ nm. We use $\theta = 65°$, $\phi = 30°$, and a broadening of $\sigma = 0.075$ eV.

the (111) direction. As this represents only the upper half of the slab, we find it reasonable to choose the thickness d of the layer ℓ to be between 5 to 10 nm. This corresponds to a half slab composed of 24 to 48 atomic layers, where we will obtain well-converged values of χ^{abc}.

In the following figures, we compare the theoretical results for the SSHG yield with the experimental results from Ref. [32]. We use $\theta = 65°$, $\phi = 30°$, and a broadening of $\sigma = 0.075$ eV. In Fig. 3, we present $\mathcal{R}_{pP}$ compared to the experimental data. With $\phi = 30°$, the contribution of χ^{xxx} from Eq. (51) is completely eliminated. First, we note that the experimental spectrum shows two very well defined resonances which come from electronic transitions from the valence to the conduction bands around the well-known $E_1 \sim 3.4$ eV and $E_2 \sim 4.3$ eV critical points of bulk Si [45]. The theoretical results reproduce the features of the spectrum, although we see that the E_2 peak is blueshifted by around 0.3 eV; details on the physics that lead to such a blueshifted theoretical spectrum are given in Ref. [30]. All the curves in this figure which include multiple reflections consider a layer thickness of $d = 10$ nm. We compare the theoretical SSHG yield for $d_2 = 0$ nm and $d_2 = 10$ nm with the SSHG yield that neglects multiple reflections. When $d_2 = 0$ nm, we have placed the polarization sheet at the bottom of the layer region. This minimizes the effect of the multiple reflections, and thus the curve is very similar to the three-layer model that neglects multiple reflections entirely. When $d_2 = 10$ nm, the polarization sheet is placed at the top of the layer region. This maximizes the effect of the multiple reflections, and therefore leads to the largest yield. We also notice that the average value obtained by using $\bar{R}_i^M$ [Eq. (22)] is intermediate between $d_2 = 0$ and $d_2 = 10$ nm, as expected. This is very similar to selecting $d_2 = d/2$, which can be interpreted as placing the nonlinear polarization sheet in the middle of the thin layer ℓ.

It is important to remark that these enhancements are larger for E_2 than for E_1. This can be understood from the fact that the corresponding λ_0 for E_1 is larger than that of E_2. From Eqs. (16), (17), and (23), we see that the phase shifts are larger for E_2 than for E_1, producing a larger enhancement of the SSHG yield at E_2 from the multiple reflections. As the phase shifts grow with d, so does the enhancement caused by the multiple reflections. We have also verified that the effects of the multiple reflections from the linear field are significantly smaller than those of the SH field. This is clear since the phase shift of Eq. (23) is not only a factor of 2 smaller than that of Eqs. (16) and (17), but also $w_\ell < W_\ell$. For larger energies, such as E_2, λ_0 becomes smaller and the multiple reflection effects become more noticeable. The selected value for $d \ll \lambda_0$, which comes naturally from the *ab initio* calculation of χ^{abc}, is thus very reasonable in order to model a thin surface layer below the vacuum region where the nonlinear SH conversion takes place.

TABLE II. Ratio of peak height (E_2/E_1) for each different curve in Fig. 3.

Label	E_2/E_1
$d_2 = 10$ nm	1.9
Average	2.0
$d_2 = 0$ nm	1.8
w/o MR	1.7
Experiment	2.8

Figure 3 shows how the inclusion of multiple reflections in the calculated SSHG yield is in better agreement with the experimental spectrum. We can further quantify the improvement by determining the yield ratio between E_2 and E_1 for each curve in Fig. 3. Table II presents these values, and we consider the maximum of each peak for both the experimental and theoretical spectra. Using the average value $\bar{R}_P^M$ yields the closest match to the experiment, while neglecting the effects of multiple reflections has the worst peak ratio. The addition of these effects does indeed improve the theoretical results, and the average value for placing the nonlinear polarization would seem to be a reasonable choice. Therefore, from this point on we will use $d = 10$ nm and $\bar{R}_i^M$ from Eq. (22) for all theoretical results that include multiple reflections.

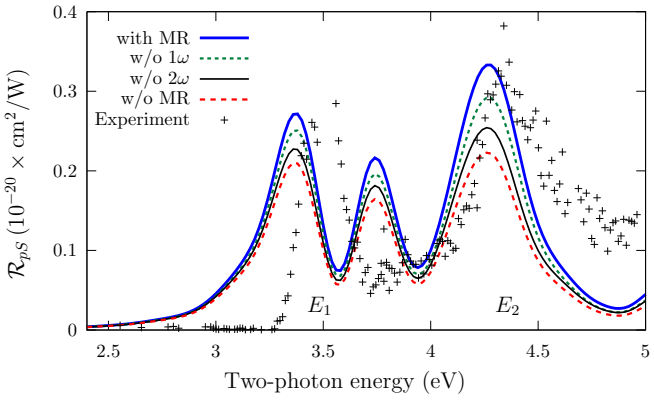

FIG. 4. Comparison of $\mathcal{R}_{pS}$ between the three-layer model with the full effect of multiple reflections (MR), without (w/o) the 2ω MR, without the 1ω MR, and without both 1ω and 2ω MR. All curves use the average value $\bar{R}_s^M$ and $d = 10$ nm for the thickness of the layer ℓ. The experimental data are taken from Ref. [32]. We use $\theta = 65°$, $\phi = 30°$, and a broadening of $\sigma = 0.075$ eV.

TABLE III. Ratio of peak height (E_2/E_1) for each different curve in Fig. 4.

Label	E_2/E_1
with MR	1.23
w/o 1ω	1.17
w/o 2ω	1.12
w/o MR	1.06
Experiment	1.34

In Fig. 4, we present $\mathcal{R}_{pS}$ compared to the experimental data; from Eq. (61), we can see that it is only proportional to the χ^{xxx} component. The theoretical curve reproduces the overall line shape of experimental results, both in position and in intensity, for the E_1 and E_2 resonant peaks; the resonance in between the two peaks is slightly overestimated by the theoretical results. In this figure, we also show the yield for the cases in which the 1ω and SH multiple reflections are neglected. We see that the overall effect in $\mathcal{R}_{pS}$ of the 1ω multiple reflections is smaller than that of the 2ω multiple reflections. As explained above, this stems from the fact of how the wavelength λ_0 enters in the multiple reflection r_p^M (1ω) and $\bar{R}_S^M$ (2ω) factors. Of course, the full 1ω and 2ω multiple reflections are equally important for the SSHG yield.

As before, we compare the yield ratio between E_2 and E_1 for the different spectra to determine which is closest to experiment. These values are presented in Table III for each curve from Fig. 4. As before, the inclusion of the effects of multiple reflections yields a theoretical spectra that has peak proportions closer to experiment. The table also provides a straightforward review of how the 1ω and 2ω terms contribute to the peak height. Again, neglecting multiple reflections produces the spectrum that is least similar to the experiment.

In Fig. 5, we present $\mathcal{R}_{sP}$ compared to the experimental data. It is clear that the effect of the multiple reflections is almost negligible. In the inset of the figure, we show the $\omega^2\Gamma_{sP}R_p^{M+}$ prefactor, which comes from Eqs. (39), (54), and (56), with and without multiple reflections. The prefactor

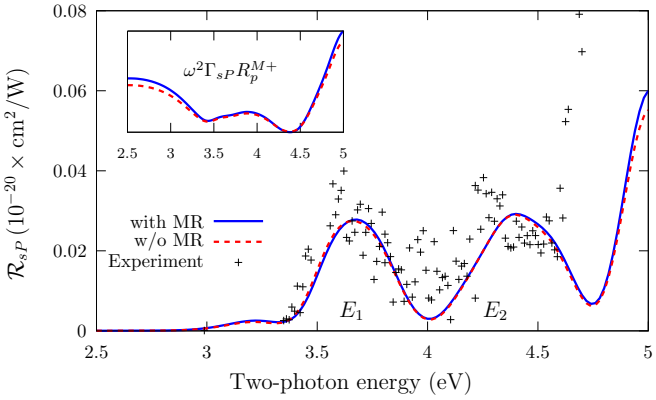

FIG. 5. Comparison of $\mathcal{R}_{sP}$ between the three-layer model with the full effect of multiple reflections (MR), and without (w/o) them. The inset shows the $\omega^2\Gamma_{sP}R_p^{M+}$ prefactor; see text for details. Experimental data are from Ref. [32]. We use $\theta = 65^\circ$, $\phi = 30^\circ$, and a broadening of $\sigma = 0.075$ eV.

is almost identical in both situations, which leads to the almost identical $\mathcal{R}_{sP}$, regardless of the effects from multiple reflections. As we compare our calculation with the experimental data, we see that both coincide well in position and in intensity. The experimental E_1 and E_2 peaks have almost the same height, and this is well reproduced in the calculated spectrum. In this case, multiple reflections do not enhance the E_2 peak with respect to the E_1 peak, as was the case for $\mathcal{R}_{pP}$ and $\mathcal{R}_{pS}$, further confirming the reliability of the three-layer model.

V. SSHG OF THE Si(001)(2 × 1) SURFACE

The Si(001)2 × 1 surface has electronic surface states that are ideal for SSHG probing. Reference [29] demonstrates how the calculation of $\chi^{\rm abc}$ for this surface can be carried out. Here, we use a scissors shift of $\hbar\Delta = 0.5$ eV that is the GW gap reported in Refs. [46] and [47]. We focus on $\mathcal{R}_{pS}$ for which we have found that there is a very well defined surface-related SH resonant peak at a two-photon energy of 1.42 eV. The Si(001)2 × 1 surface reconstruction yields a class 1 primitive triclinic system with all the 12 components required by $\mathcal{R}_{pS}$ [Eq. (60)] independent from each other [48]. Therefore, we cannot take advantage of any symmetry relations for this surface. However, this is no problem for the versatile formulation we derived in Sec. III which can accommodate all 12 components disregarding any surface symmetries. The reconstruction of the Si(001)2 × 1 surface is characterized by a dimer along the [011] crystallographic direction that corresponds to x in our Cartesian system [29].

In Fig. 6 we show $\mathcal{R}_{pS}$ for two different cases. In the first, we take $\mathcal{R}_{pS}$ vs ϕ for a fixed $\theta_0 = 10^\circ$, and in the second, vs θ_0 for a fixed $\phi = 90^\circ$. We notice a very intense SSHG yield around $2\hbar\omega \sim 1.4$ eV, with less intense structures above ∼2.5 eV. The former is the surface-related SH resonance, and the latter are the resonant peaks related to the E_1 and E_2 critical points of Si. From this figure, we see that the best conditions for measurement are for $\phi = 90^\circ$ with a small angle of incidence θ_0. This azimuthal angle corresponds to incidence of the fundamental electric field (with p polarization) perpendicular to the surface dimers, and it is quite interesting to notice that for illumination along the dimers ($\phi = 0^\circ$ or 180°), $\mathcal{R}_{pS} \sim 0$. To understand this behavior, we obtain from Eq. (60) that

$$r_{pS}[\phi = 90^\circ] = -\left(r_p^{M-}\right)^2 w_\ell^2 \chi^{xyy} - 2r_p^{M+} r_p^{M-} w_\ell \sin\theta_0 \chi^{xzy} - \left(r_p^{M+}\right)^2 \sin^2\theta_0 \chi^{xzz}, \quad (69)$$

and likewise

$$r_{pS}[\phi = 0^\circ] = \left(r_p^{M-}\right)^2 w_\ell^2 \chi^{yxx} + 2r_p^{M+} r_p^{M-} w_\ell \sin\theta_0 \chi^{yxz} + \left(r_p^{M+}\right)^2 \sin^2\theta_0 \chi^{yzz}. \quad (70)$$

The calculation of $\chi^{\rm abc}$ [29] results in $|\chi^{yxx}| \sim |\chi^{yxz}| \sim |\chi^{yzz}| \sim |\chi^{xzy}| \ll |\chi^{xzz}| \sim |\chi^{xyy}|$. For incoming fields along the dimers, $\mathcal{R}_{pS}$ is very small, not because of symmetry reasons that could cause $\chi^{yxx} = \chi^{yxz} = \chi^{yzz} = 0$, but from the electronic structure of the surface that leads to values that are less than 1.4% of the χ^{xyy} and χ^{xzz} components involved when the incoming fields are perpendicular to the dimers. Both the $\phi = 0^\circ$ and $\phi = 90^\circ$ results can be easily understood from the intuitive fact that the dimer is more

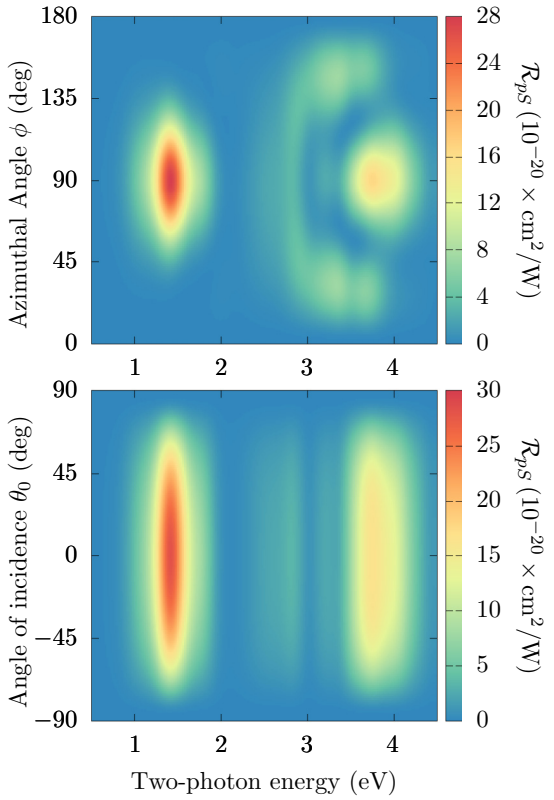

FIG. 6. $\mathcal{R}_{pS}$ vs two-photon energy vs ϕ for a fixed $\theta = 10^\circ$ (top panel), and vs θ_0 for a fixed $\phi = 90^\circ$ (bottom panel), for the Si(001)(2 × 1) surface.

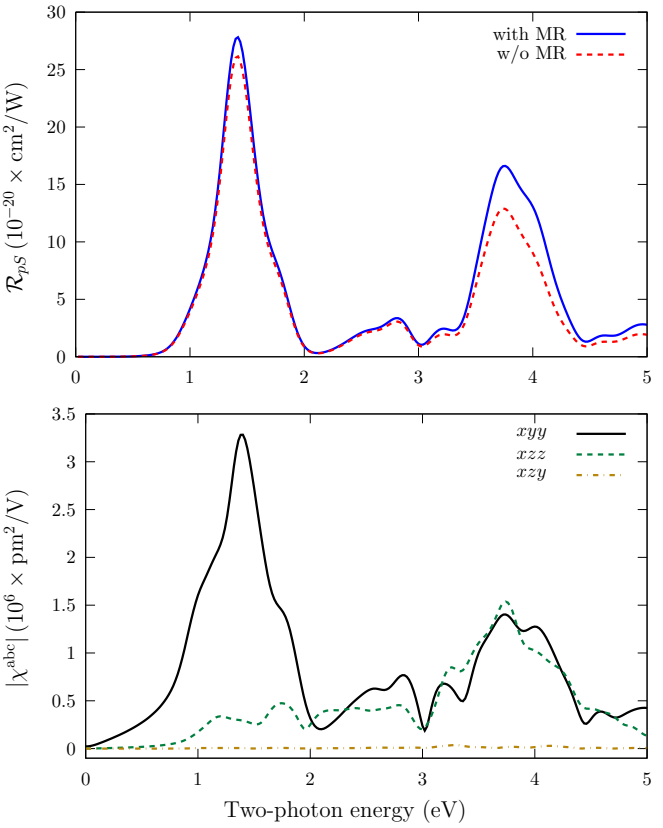

FIG. 7. The top panel shows $\mathcal{R}_{pS}$ for $\theta_0 = 10^\circ$ and $\phi = 90^\circ$ for the Si(001)(2 × 1) surface. The bottom panel shows the components of χ^{abc} involved in $\mathcal{R}_{pS}$.

prone to be polarized along its length than across it. For $\phi = 0^\circ$, $\mathcal{R}_{pS}$ involves χ^{ybc} components, and the nonlinear polarization $\mathcal{P}$ will point only along y (perpendicular to the dimer). For $\phi = 90^\circ$, the χ^{xbc} components are the ones that contribute, and these give a nonlinear polarization $\mathcal{P}^x$ which points along the dimer, and thus much larger than $\mathcal{P}^y$. Recall that the nonlinear process mixes the direction of the exciting electric fields with the outgoing direction of the nonlinear polarization. Therefore, we clearly see that what is important is not the direction of excitation along or across the dimer, but rather how the direction of the nonlinear polarization is induced by the nonzero Cartesian components of χ^{abc}. This result constitutes a clear example of what nonlinear optics is all about.

We narrow our focus onto a particular spectrum to gain insight into these results. In Fig. 7 we present $\mathcal{R}_{pS}$ for $\phi = 90^\circ$ and $\theta_0 = 10^\circ$, where we see a very well defined surface SH peak at $2\hbar\omega = 1.42$ eV, with an intensity 17 times larger than that of the E_2 peak for $\mathcal{R}_{pP}$ from the Si(111)1 × 1:H surface (see Fig. 3). We notice that there are no E_1 and E_2 single peaks, but instead there is a mixture of both resonances that produce a rather wide peak between these values. Also, we see that the effect of multiple reflections is larger for higher energies as discussed previously with the Si(111)1 × 1:H surface. From the bottom panel of the figure we see that the surface SH peak mainly comes from χ^{xyy}. The bulk SH peak is a mixture of the χ^{xyy} and χ^{xzz} components, and χ^{xzy} is negligible. This could be geometrically interpreted as follows. χ^{xyy} has Cartesian components only along the surface; thus, it mainly has surface-related information. On the other hand, χ^{xzz} has "depth" (z) components; thus, it mainly has bulk-related features. Of course, χ^{xyy} and χ^{xzz} have both bulk and surface information, which manifests itself at the surface due to the surface's noncentrosymmetric environment.

Finally, we follow Ref. [29] in order to calculate the layer-by-layer contribution to χ^{xyy}. Each layer in the Si(001)2 × 1 supercell contains two Si atoms. In Fig. 8, we show the contribution to Im[χ^{xyy}] coming from the first (topmost) layer

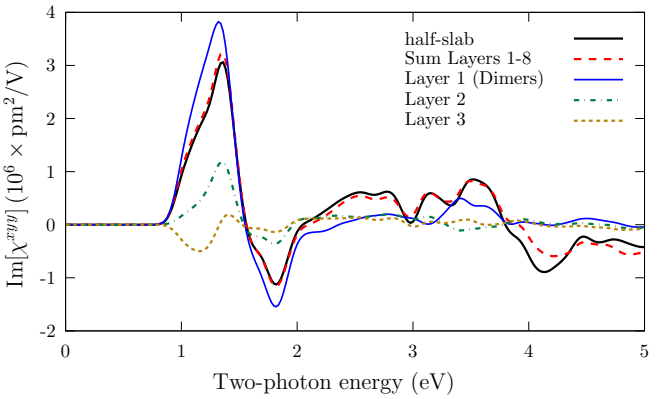

FIG. 8. Layer-by-layer decomposition of Im[χ^{xyy}] for the Si(001)(2 × 1) surface (see text for details).

that contains the dimer, the contributions from the second and third layers, and the sum of the first eight layers. We also include $\mathrm{Im}[\chi^{xyy}_{\text{half-slab}}]$, which according to Ref. [29] is the surface value of $\mathrm{Im}[\chi^{xyy}]$. It is this "half-slab" value for χ^{abc} that we use in our formulation for the SSHG yield, presented above. As we compare against $\mathrm{Im}[\chi^{xyy}_{\text{half-slab}}]$, we see that $\mathrm{Im}[\chi^{xyy}_{\text{dimer}}]$ accounts for most of the surface SH peak at 1.42 eV. The second layer also has a small contribution to this peak. The third layer has an even smaller positive contribution, but also a negative part that subtracts from the total peak intensity. These negative contributions are such that as we add the first eight layers, we obtain that $\mathrm{Im}[\chi^{xyy}_{\text{layer 1-8}}] \sim \mathrm{Im}[\chi^{xyy}_{\text{half-slab}}]$; the latter includes 16 layers (representing half of the total slab). In general, the contributions from the different layers could have opposite signs that diminish the contribution of any one layer towards the half-slab or surface value of $\boldsymbol{\chi}$. Conversely, a given SH peak can be enhanced by different layers if those layers produce contributions with the same sign. Therefore, the layer-by-layer analysis demonstrates that the predicted SH surface peak primarily comes from the Si dimers right at the surface of the Si(001)2 × 1 reconstruction. This is yet another example of the great surface sensitivity of SSHG.

VI. CONCLUSIONS

We have derived the complete expressions for the SSHG yield using the three-layer model to describe the radiating system. This treatment includes the effects of multiple reflections inside the material from both the SH and fundamental fields. Our derivation yields the full expressions for the yield for the commonly used incoming and outgoing s and p polarizations, and can include all the required components of χ^{abc}, regardless of symmetry considerations; thus, these expressions can be applied to any surface symmetry. We also reduce them according to the most commonly used surface symmetries, the (111), (110), and (001) cases.

The results obtained from using the theory developed here were applied to the Si(111)(1 × 1):H surfaces. Our three-layer model accurately reproduces key spectral features and yields an intensity very close to experiment for all the cases studied. We consider it an upgrade over the much reviewed two-layer model [21], and it comes with very little added computational expense. The addition of the effects of multiple reflections either enhances the intensity of the calculated spectra and improves the peak proportions, or has little effect at all, always in close agreement with experiment.

We also presented a predictive study of the SSHG yield from the Si(001)(2 × 1) surface. As mentioned above, our robust formulation can accommodate all 18 independent components (for SHG) of χ^{abc} for any surface, and we focused on $\mathcal{R}_{pS}$ which uses 12 of these components. We find clear evidence of electronic surface states around a two-photon energy of 1.41 eV, and we present a brief overview of the produced SSHG yield over a wide range of incident (θ_0) and azimuthal (ϕ) angles, along with a physical understanding of the results. This type of plot will be quite useful to the experimentalist interested in this kind of spectroscopy. Overall, our theoretical three-layer model can be used to quantitatively study the SSHG yield.

ACKNOWLEDGMENTS

B.S.M. acknowledges partial support from CONACYT-México Grant No. 153930. S.M.A. gratefully acknowledges full support from CONACYT-México Scholarship No. 349278.

[1] C. K. Chen, A. R. B. de Castro, and Y. R. Shen, Surface-Enhanced Second-Harmonic Generation, Phys. Rev. Lett. **46**, 145 (1981).

[2] Y. R. Shen, Surface properties probed by second-harmonic and sum-frequency generation, Nature (London) **337**, 519 (1989).

[3] J. F. McGilp, M. Cavanagh, J. R. Power, and J. D. O'Mahony, Probing semiconductor interfaces using nonlinear optical spectroscopy, Opt. Eng. **33**, 3895 (1994).

[4] N. Bloembergen, Surface nonlinear optics: A historical overview, Appl. Phys. B **68**, 289 (1999).

[5] J. F. McGilp, Second-harmonic generation at semiconductor and metal surfaces, Surf. Rev. Lett. **06**, 529 (1999).

[6] G. Lüpke, Characterization of semiconductor interfaces by second-harmonic generation, Surf. Sci. Rep. **35**, 75 (1999).

[7] M. C. Downer, Y. Jiang, D. Lim, L. Mantese, P. T. Wilson, B. S. Mendoza, and V. I. Gavrilenko, Optical second harmonic spectroscopy of silicon surfaces, interfaces and nanocrystals, Phys. Status Solidi A **188**, 1371 (2001).

[8] M. C. Downer, B. S. Mendoza, and V. I. Gavrilenko, Optical second harmonic spectroscopy of semiconductor surfaces: Advances in microscopic understanding, Surf. Interface Anal. **31**, 966 (2001).

[9] C. W. van Hasselt, M. A. C. Devillers, Th. Rasing, and O. A. Aktsipetrov, Second-harmonic generation from thick thermal oxides on Si(111): The influence of multiple reflections, J. Opt. Soc. Am. B **12**, 33 (1995).

[10] William S. Kolthammer, Dustin Barnard, Nicole Carlson, Aaron D. Edens, Nathan A. Miller, and Peter N. Saeta, Harmonic generation in thin films and multilayers, Phys. Rev. B **72**, 045446 (2005).

[11] M. S. Yeganeh, J. Qi, J. P. Culver, A. G. Yodh, and M. C. Tamargo, Interference in reflected second-harmonic generation from thin nonlinear films, Phys. Rev. B **46**, 1603 (1992).

[12] Y. Hase, K. Kumata, S. S. Kano, M. Ohashi, T. Kondo, R. Ito, and Y. Shiraki, New method for determining the nonlinear optical coefficients of thin films, Appl. Phys. Lett. **61**, 145 (1992).

[13] G. Buinitskaya, I. Kravetsky, L. Kulyuk, V. Mirovitskii, and E. Rusu, Optical second harmonic generation in ZnO film: Multiple-reflection effects, Moldavian Journal of the Physical Sciences **1**(N4), 77 (2002).

[14] G. Buinitskaya, I. Kravetsky, L. Kulyuk, V. Mirovitskii, and E. Rusu, Characterization of thin ZnO film by optical second harmonic generation: Experiment and theory, in *Semiconductor Conference, 2003: CAS 2003, International*, Vol. 2 (IEEE Service Center, Piscataway, NJ, 2003), p. 322.

[15] P. D. Maker, R. W. Terhune, M. Nisenoff, and C. M. Savage, Effects of Dispersion and Focusing on the Production of Optical Harmonics, Phys. Rev. Lett. **8**, 21 (1962).

[16] G. Tellier and C. Boisrobert, Second harmonic generation: Effects of the multiple reflections of the fundamental and the second harmonic waves on the Maker fringes, Opt. Commun. **279**, 183 (2007).

[17] M. Abe, I. Shoji, J. Suda, and T. Kondo, Comprehensive analysis of multiple-reflection effects on rotational Maker-fringe experiments, J. Opt. Soc. Am. B **25**, 1616 (2008).

[18] N. Bloembergen and P. S. Pershan, Light waves at the boundary of nonlinear media, Phys. Rev. **128**, 606 (1962).

[19] B. Dick, A. Gierulski, G. Marowsky, and G. A. Reider, Determination of the nonlinear optical susceptibility $\chi^{(2)}$ of surface layers by sum and difference frequency generation in reflection and transmission, Appl. Phys. B **38**, 107 (1985).

[20] J. E. Sipe, D. J. Moss, and H. M. van Driel, Phenomenological theory of optical second- and third-harmonic generation from cubic centrosymmetric crystals, Phys. Rev. B **35**, 1129 (1987).

[21] V. Mizrahi and J. E. Sipe, Phenomenological treatment of surface second-harmonic generation, J. Opt. Soc. Am. B **5**, 660 (1988).

[22] M. Cini, Simple model of electric-dipole second-harmonic generation from interfaces, Phys. Rev. B **43**, 4792 (1991).

[23] R. Morita, T. Kondo, Y. Kaneda, A. Sugihashi, N. Ogasawara, S. Umegaki, and R. Ito, Multiple-reflection effects in optical second-harmonic generation, Jpn. J. Appl. Phys. **27**, L1134 (1988).

[24] F. Goos and H. Hänchen, Ein neuer und fundamentaler Versuch zur Totalreflexion, Ann. Phys. **436**, 333 (1947).

[25] H. Shih and N. Bloembergen, Phase-matched critical total reflection and the Goos-Haenchen shift in second-harmonic generation, Phys. Rev. A **3**, 412 (1971).

[26] V. J. Yallapragada, A. P. Ravishankar, G. L. Mulay, G. S. Agarwal, and V. G. Achanta, Observation of giant Goos-Hänchen and angular shifts at designed metasurfaces, Sci. Rep. **6**, 19319 (2016).

[27] V. J. Yallapragada, Achanta Venu Gopal, and G. S. Agarwal, Goos-Hänchen shifts in harmonic generation from metals, Opt. Express **21**, 10878 (2013).

[28] L. Reining, R. Del Sole, M. Cini, and J. G. Ping, Microscopic calculation of second-harmonic generation at semiconductor surfaces: As/Si(111) as a test case, Phys. Rev. B **50**, 8411 (1994).

[29] S. M. Anderson, N. Tancogne-Dejean, B. S. Mendoza, and V. Véniard, Theory of surface second-harmonic generation for semiconductors including effects of nonlocal operators, Phys. Rev. B **91**, 075302 (2015).

[30] S. M. Anderson, N. Tancogne-Dejean, B. S. Mendoza, and V. Véniard, Improved *ab initio* calculation of surface second-harmonic generation from Si(111)(1 × 1)H, Phys. Rev. B **93**, 235304 (2016).

[31] J. E. Mejía, C. Salazar, and B. S. Mendoza, Layer-by-layer analysis of second harmonic generation at a simple surface, Revista Mexicana de Física **50**, 134 (2004).

[32] J. E. Mejía, B. S. Mendoza, M. Palummo, G. Onida, R. Del Sole, S. Bergfeld, and W. Daum, Surface second-harmonic generation from Si(111)(1 × 1)H: Theory versus experiment, Phys. Rev. B **66**, 195329 (2002).

[33] O. A. Aktsipetrov, I. M. Baranova, and Yu. A. Il'inskii, Surface contribution to the generation of reflected second-harmonic light for centrosymmetric semiconductors, Zh. Eksp. Teor. Fiz. **91**, 287 (1986) [J. Exp. Theor. Phys. **64**, 167 (1986)].

[34] Z. Xu, X. F. Hu, D. Lim, J. G. Ekerdt, and M. C. Downer, Second harmonic spectroscopy of Si(001) surfaces: Sensitivity to surface hydrogen and doping, and applications to kinetic measurements, J. Vac. Sci. Technol. B **15**, 1059 (1997).

[35] P. Guyot-Sionnest and Y. R. Shen, Bulk contribution in surface second-harmonic generation, Phys. Rev. B **38**, 7985 (1988).

[36] Y. R. Shen, Surface contribution versus bulk contribution in surface nonlinear optical spectroscopy, Appl. Phys. B **68**, 295 (1999).

[37] R. W. Boyd, *Nonlinear Optics* (Academic Press, New York, 2003).

[38] Richard L. Sutherland, *Handbook of Nonlinear Optics* (CRC Press, Boca Raton, 2003).

[39] J. E. Sipe, New Green's function formalism for surface optics, J. Opt. Soc. Am. B **4**, 481 (1987).

[40] J. D. Jackson, *Classical Electrodynamics*, 3rd ed. (Wiley-VCH, Berlin, 1998).

[41] S. M. Anderson, Theoretical optical second-harmonic calculations for surfaces, Ph.D. thesis, Centro de Investigaciones en Óptica, A.C., 2016.

[42] S. A. Mitchell, M. Mehendale, D. M. Villeneuve, and R. Boukherroub, Second harmonic generation spectroscopy of chemically modified Si(1 1 1) surfaces, Surf. Sci. **488**, 367 (2001).

[43] S. Bergfeld, B. Braunschweig, and W. Daum, Nonlinear Optical Spectroscopy of Suboxides at Oxidized Si(111) Interfaces, Phys. Rev. Lett. **93**, 097402 (2004).

[44] Y. Li and G. Galli, Electronic and spectroscopic properties of the hydrogen-terminated Si(111) surface from *ab initio* calculations, Phys. Rev. B **82**, 045321 (2010).

[45] P. Yu and M. Cardona, *Fundamentals of Semiconductors: Physics and Materials Properties*, 3rd ed. (Springer Science & Business Media, Berlin, 2005).

[46] M. Rohlfing, P. Krüger, and J. Pollmann, Efficient scheme for *GW* quasiparticle band-structure calculations with applications to bulk Si and to the Si(001)-(2 × 1) surface, Phys. Rev. B **52**, 1905 (1995).

[47] P. García-González and R. W. Godby, *GW* self-energy calculations for surfaces and interfaces, Comput. Phys. Commun. **137**, 108 (2001).

[48] S. V. Popov, Y. P. Svirko, and N. I. Zheludev, *Susceptibility Tensors for Nonlinear Optics*, Series in Optics and Optoelectronics (CRC Press, Boca Raton, 1995).